

# EXPERIMENTAL CHARACTERIZATION AND STOCHASTIC MODELING OF INTERLAMINAR SHEAR STRENGTHS OF GRAPHITE/EPOXY LAMINATED COMPOSITES

Chao Zhang, R. Ganesan and Suong V. Hoa

*Concordia Centre for Composites, Department of Mechanical Engineering  
Concordia University  
Montreal, Quebec, Canada H3G 1M8*

**SUMMARY:** The experimental and analytical investigations are conducted concerning the effects of fiber orientations on the interlaminar shear (ILS) strengths in laminated composites. The modified double notch shear test is employed in the experiment, and a stochastic modeling technique is developed in the analysis. It is found that both the mean values and probability distribution forms of the interlaminar shear strengths vary with the fiber orientation difference between the two surrounding plies of the interfaces.

**KEYWORDS :** delamination, fracture, interlaminar shear specimen (ILSS)

## 1. INTRODUCTION

Delamination failure of laminated composites can be predicted by two distinct methodologies; one based on fracture mechanics, and the other based on mechanics of materials. The fracture mechanics approach employs the delamination criteria that are in terms of strain energy release rates. Therefore, the release rates need to be calculated and then are compared with their critical values in those criteria. The mechanics of materials approach makes use of stress-based delamination criteria and thus a local 3D stress analysis is necessary. The Mode I, Mode II and Mode III critical strain energy release rates in the fracture mechanics approach and the interlaminar shear and normal strength components in the mechanics of materials approach can be considered as material properties, which characterize the resistance of composite materials against delamination. Recently, the effects of fiber orientations in laminated composites on the Mode II critical release rates ( $G_{IIC}$ ) have been extensively studied using the end notch flexure (ENF) testing technique [1-4]. The experimental results seem to demonstrate two contrasting conclusions, concerning whether the  $G_{IIC}$  at the interfaces depend on the fiber orientations of their surrounding plies. Apparent dependence was reported, such as by Chou et al [1], and Tao and Sun [2]. However little dependence was also reported, such as by Russell and Street [3], and Davidson et al. [4].

Although so much experimental work has been executed pertaining to the effects of fiber orientations on the  $G_{IIC}$  in laminated composites, the corresponding effects on the ILS strengths have never so far been investigated. More recently, a systematic investigation is being performed at the Concordia Centre for Composites, which consists of four aspects: 1) development of analytical solutions towards the 3D stress state in laminated composites, with straight free edges, unloaded hole edges, and pin-loaded hole edges with and without friction [5-7]; 2) experimental quantification and stochastic modeling of the effects of fiber orientations on the interlaminar shear

and normal strengths; 3) development of delamination criteria in terms of interlaminar strengths that are dependent on the fiber orientations; and 4) probabilistic evaluation of the delamination failure on the basis of the developed stress-based criteria. The present paper describes the experimental program, and reports the experimental results and stochastic modeling of the ILS strengths.

## 2. EXPERIMENTAL CHARACTERIZATION OF ILS STRENGTHS

Two ILS strength components that are normal to each other are essential, if the stress-based criteria are employed to characterize the delamination failure [8]. Hence, experiments based on the double notch shear testing technique are performed on the laminated composite specimens with  $0/\theta$  and  $90/(90-\theta)$  interfaces, in order that the fiber orientation difference (FOD) angle between the two surrounding plies always equals to  $\theta$ . Corresponding to these two types of interfaces, the ILS strength components are defined as  $S_{13}$  and  $S_{23}$ . The specimen lay-ups are

Specimens (Type I) for  $S_{13}$ :  $[(0/\theta)_3/(\theta/0)_3]/[(\theta/0)_3/(0/\theta)_3]$

Specimens (Type II) for  $S_{23}$ :  $[(90/(90-\theta))_2/0_4/((90-\theta)/90)_2]/[(90-\theta)/90)_2/0_4/(90/(90-\theta))_2]$

where  $\theta = 0^\circ, 10^\circ, 20^\circ, 30^\circ, 40^\circ, 50^\circ, 60^\circ, 70^\circ, 80^\circ$  and  $90^\circ$ . The reasons that the above lay-ups are arranged will be given in the coming sections. The CYTEC® G40-800/5276-1 carbon/epoxy tapes with a nominal thickness of 0.185 mm are employed in our experimental program due to their extensive aerospace application. Because of the considerable scatter in the interlaminar strengths, every data set at each specified interface is obtained by testing 35 effective specimens, so that the  $\theta$ -dependence of ILS strengths is expected not to be masked by the scatter.

### 1) TESTING SETUP

The double notch shear test, suggested in ASTM Standard D 3846 for the unidirectional specimens, is modified so that it can be employed to properly characterize the ILS strengths of laminated specimens. The specimens have to contain unsymmetric stacking sequences, because the effects of fiber orientations on the ILS strengths must be experimentally quantified from the specified interfaces located at the specimen central planes. Compared with the unidirectional specimens, the unsymmetric specimens pose a number of special problems. These problems will be addressed based on a detailed 3D finite element stress analysis.

Due to the two asymmetrical notches, an undesirable bending moment would appear in the specimens. Moreover, since the matrix tensile strength may be lower than the ILS strengths, a tensile load would cause transverse matrix cracks prior to the delamination onset. Hence, a compressive load is applied to the specimens that are held between a steel clamp by tightened bolts, as shown in Fig. 1. The clamp not only prevents the specimens from bending, but also exerts a compressive pressure on the specimens by evenly tightening the bolts. The transverse pressure can reduce or remove the interlaminar tensile stress, thus partially eliminating the possibility of delamination induced by the free edge effects. With the clamp, the notch width has little effect on the measured ILS strengths. Thus the selection of the notch width can be within a small range;  $w = 1.8$  mm is selected. The ratio of notch space to specimen thickness (i.e.,  $s/t$ ) has significant effects on the ILS stress distribution in the specimen gauge sections, and thus the measured ILS strengths. The smaller the ratio of  $s/t$ , the more uniform the ILS stress  $\tau_{xz}$  is at the central planes. A notch space  $s = 7$  mm is selected, and 24 plies are used to stack the specimens with a nominal thickness  $t = 4.44$  mm. The notch depth  $d$  also seems to be an important parameter. Chiao et al. [9] reported that the measured ILS strengths depend on the notch depth. For example, a slight undercut ( $d < t/2$ ) could give a high strength than an overcut ( $d > t/2$ ) because of the fiber tearing in the undercut specimens. Shokrieh et al. [10] argued that if a clamp is used, a slight change of the notch depth has little effect on the measured ILS strengths. Our 3D finite element results show that the undercut with one ply thickness does have a little effect on the stress distribution inside the specimen gauge

sections, but the effects of the overcut is less. Therefore, we suggest that it be necessary to reduce or remove the undercut in order to yield the good experimental data for the ILS strengths.

The geometry and nominal dimensions for the specimens are given in Fig. 2. The notch shape is modified; the notch bottoms are designed to be of round shape with a fillet radius of 0.9 mm. This modification can make it convenient to cut the notches using a diamond blade instead of a milling bit. A 2D stress analysis is conducted on the unidirectional specimens using the ANSYS finite element software [11], and the fillets are considered in order to observe the influence on the stress distribution. The stress analysis results are shown in Fig. 3, where the  $\tau_{xz}$  is demonstrated with respect to the transformed axis  $\xi = (x - L)/s$  at the central plane. It can be seen that the fillets do affect the stress distribution; the  $\tau_{xz}$  is maximum and immediately drops down at the tips of the notches without fillets, while maximum a little away from the notches and then drops down inside the fillet regions. Thus the nominal uniform ILS stress at the central planes is modified as

$$\tau_{xz}^0 = \frac{P}{b(s + 2\delta)} \quad (1)$$

where  $P$  is the applied load and  $\delta$  is a correction parameter; for non-filletted specimens,  $\delta = 0$ , and for filletted specimens, the best selection is found to be  $\delta = 0.5$  mm for the geometry specified here. This means that the materials inside the fillet regions can carry a part of the external load. The ILS strengths are thus calculated by substituting the measured ultimate load into Equ 1. The  $\tau_{xz}$  shown in Fig. 3 is normalized with respect to the  $\tau_{xz}^0$  in each case.



**Fig. 1.** The double notch shear testing setup.

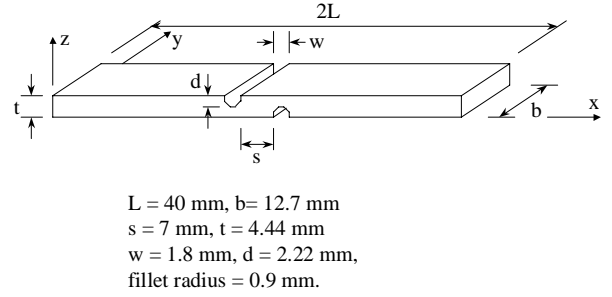


**Fig. 2.** The specimen geometry.

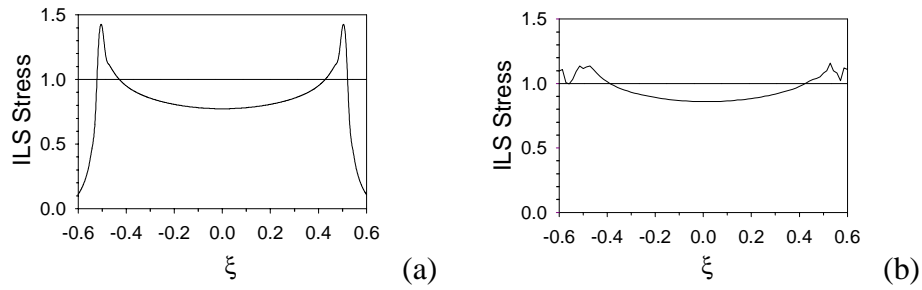


**Fig. 3.** Distributions of the  $\tau_{xz}$  at the central planes in a) non-filletted and b) filletted specimens.

## 2) SPECIMEN LAY-UP DESIGN AND FINITE ELEMENT ANALYSIS

A 3D stress analysis using ANSYS software [11] is performed on the clamped specimens. The specimens are modeled using the 8-node 3D layered structural solid elements. For reasons of convenience, the 3D stress analysis is only performed on the non-filletted specimens due to the difficulty in meshing the fillet regions using the layered elements. The lay-ups have similar effects on the stress distribution in these two types of specimens, especially in the width ( $y$ ) direction. So it is reasonable to judge the effects in the filletted specimens based on the stress distribution in the non-filletted specimens. The non-filletted specimens are meshed into 3960 layered elements.

The  $[(0/\theta)_3/(\theta/0)_3//(\theta/0)_3/(0/\theta)_3]$  lay-up is arranged for the Type I specimens. The numerical results based on the Classical Lamination Theory show that there are no coupling effects of bending and twisting in such a type of lay-up. A number of  $0/\theta$  interfaces around the central planes can insure that delamination always takes place at a  $0/\theta$  interface even though the notches are not cut precisely to half the specimen thickness. The  $0^\circ$  and  $\theta$  plies are alternatively arranged in order to reduce the free edge effects. It is important that the above lay-up is arranged for the specimens rather than the  $[(\beta/-\beta)_3/(-\beta/\beta)_3//(-\beta/\beta)_3/(\beta/-\beta)_3]$  lay-up ( $\beta = \theta/2$ ) usually used in the ENF test for  $G_{IIC}$  [4]. The major reason is that the designed lay-up can greatly reduce the free edge effects in the specimens, thereby providing the uniform stress distribution. Moreover, the in-plane shear stress  $\tau_{12}$  along the fiber direction is much smaller in the central plies of the designed specimens, which is desired because it can reduce the possibility of transverse matrix cracks.

At first, the  $[(90/\beta)_3/(\beta/90)_3//(\beta/90)_3/(90/\beta)_3]$  lay-up ( $\beta = 90^\circ - \theta$ ) was naturally selected for the Type II specimens. The tests on the  $[90]_{24}$  and  $[(90/80)_3/(80/90)_3//(\theta/90)_3/(90/80)_3]$  specimens used to be performed to attempt the  $S_{23}$  at the  $90/90$  and  $90/80$  interfaces. The matrix compressive failure, unfortunately, took place inside the notched parts instead of the desired delamination at the central planes. The deadlock could be removed by replacing a number of  $90^\circ$  plies by the  $0^\circ$  plies, but the disadvantage involves that delamination would be initiated at the  $0/90$  or  $0/(90-\theta)$  interfaces rather than at the  $90/(90-\theta)$  interfaces. However, the inclusion of some  $0^\circ$  plies can provide a more uniform distribution of the  $\tau_{xz}$  in the specimen gauge sections. Therefore, this solution is accepted in our experimental program, so that the Type II specimens contain a  $[(90/\beta)_2/0_4/(\beta/90)_2//(\beta/90)_2/0_4/(90/\beta)_2]$  lay-up ( $\beta = 90^\circ - \theta$ ). The experimental data from the specimens initially delaminated at the  $0/90$  or  $0/(90-\theta)$  interfaces are discarded, so more specimens will be prepared and tested. The numerical results from the Classical Lamination Theory also show that no coupling effects of bending and twisting appear in such type of lay-up.

### 3) SPECIMEN PREPARATIONS AND TESTING PROCEDURE

The laminates are cured in an autoclave following a specified curing cycle. The quality of the cured laminates is examined by a C-Scan non-destructive technique. The half-thickness notches are cut using a diamond blade wheel with a higher grit order; the tolerance of notch depth is allowed to be less than one ply thickness. After the specimens are cut from the laminates by a diamond blade wheel, the edges are ground using the sandpapers with grit orders of 120 and 320 respectively to remove the potential cutting damage. The specimens are clipped into the clamp by applying a torque of 1 lb<sub>f</sub>. in. through a torque wrench, and then mounted on a MTS testing machine. The compressive load is formed by moving the steel platen upward at a constant speed of 1 mm/min. and terminated when the load suddenly drops down close to zero.

### 4) EXPERIMENTAL RESULTS AND DISCUSSIONS

As expected, all the Type I specimens are delaminated around the central planes, and some Type II specimens initiate the delamination at the  $0/90$  or  $0/(90-\theta)$  interfaces rather than at the intended  $90/(90-\theta)$  interfaces around the central planes. These ineffective specimens are discarded and therefore more specimens are tested until the 35 effective specimens are obtained. Fortunately, only a limited number of ineffective specimens appear in testing the  $S_{23}$  at the  $90/90$  and  $90/80$  interfaces, but few ineffective specimens appear with the other interfaces. The load versus displacement curves for all the specimens exhibit a linear response until failure.

#### 4.1. Statistical Analysis of ILS Strengths

The mean values  $\mu$  and standard deviations for the measured  $S_{13}$  at the 10 specified interfaces, represented by the bars and error bars, are shown in Fig. 4. It is apparent that both  $\mu$  and coefficients of variation  $C_v$  strongly depend on the angle  $\theta$ . The  $S_{13}$  reaches the maximum around  $\theta = 60^\circ$  and the minimum around  $\theta = 80^\circ$ ; the maximum value is 69.3% larger than the

minimum value. The  $C_v$  is found to be quite large except for at  $\theta = 60^\circ$  and  $90^\circ$ . The mean values and standard deviations for the measured  $S_{23}$  at the 10 specified interfaces are also shown in Fig. 4. Compared with the  $S_{13}$ , the dependence of these probabilistic parameters on  $\theta$  for the  $S_{23}$  is not so strong. The  $S_{23}$  reaches the maximum around  $\theta = 40^\circ$  and the minimum around  $\theta = 70^\circ$ ; the maximum value is 30.7% larger than the minimum value. The  $C_v$  for the  $S_{23}$  is found to be smaller, and  $\mu$  is higher than that for the  $S_{13}$  except at  $\theta = 60^\circ$ . It is likely that the  $90^\circ$  plies form an obstacle against the delamination growth, thus increasing the  $S_{23}$  and decreasing the  $C_v$  [4].

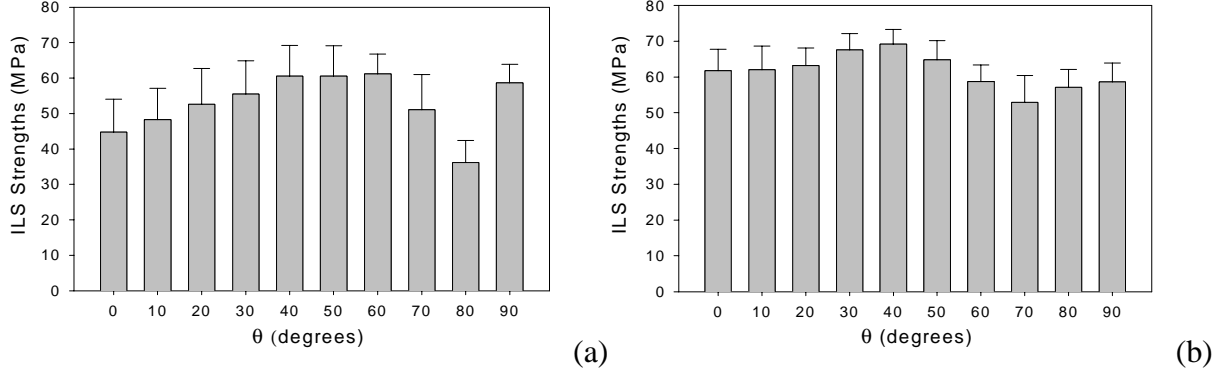


**Fig. 4.** Experimental results of the ILS strengths vs the FOD angle  $\theta$ ; a)  $S_{13}$  and b)  $S_{23}$ .

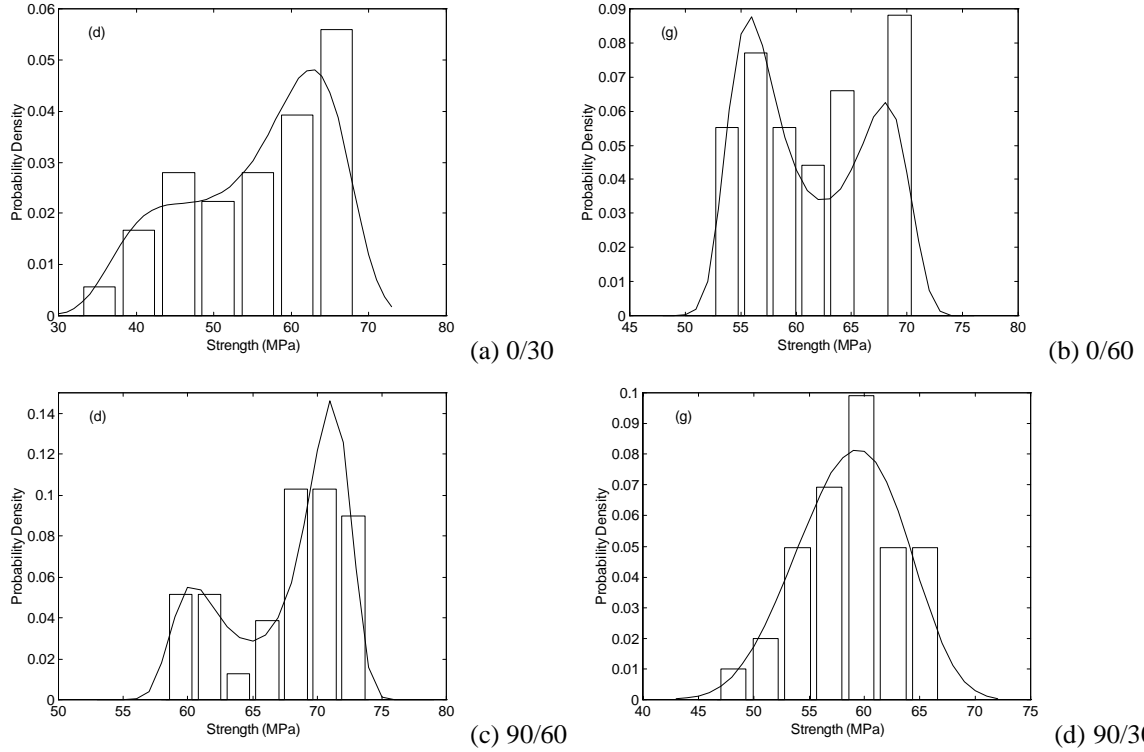


**Fig. 5.** Histograms and maximum entropy pdfs of the ILS strengths; a)  $S_{13}$  at 0/30 interface, b)  $S_{13}$  at 0/60 interface, c)  $S_{23}$  at 90/60 interface, and d)  $S_{23}$  at 90/30 interface.

The histograms of the measured ILS strengths demonstrate that their randomness does not follow the Gaussian or Weibull distributions. Therefore, it is essential to describe the individual probability density functions (pdfs) using an analytical distribution. The maximum entropy technique [12] is thus used to treat the experimental data, which represents the pdfs in a general form as

$$f(s) = \exp[\lambda_0 + \sum_{i=1}^p \lambda_i s^i] \quad (2)$$

where  $\lambda_i$ 's, and  $i = 0, 1, \dots, p$ , are the parameters to be determined from the given sample data sets. The salient features in Equ 2 are that the form of the pdfs is given a priori. Thus, the parameters  $\lambda_i$ 's can be evaluated by the low and high bounds and the moments up to the  $p$ -th order of the random variables. The order  $p = 4$  is found to be adequate to characterize the individual pdfs of the measured ILS strengths. The low and high bounds of each data set are determined by a tentative process. The good selection is found that the low bound equals to 0.92 minimum strength value and the high bound to 1.08 maximum strength value in each experimental data set. Due to space limitation, the histograms and the individual pdfs for the  $S_{13}$  only at the 0/30 and 0/60 interfaces, and for the  $S_{23}$  only at the 90/60 and 90/30 interfaces, are presented in Fig. 5. Apparent differences are observed between the individual pdfs at each specified interface, therefore the probability distribution forms also change with  $\theta$ .

#### 4.2. Fracture Surface Morphologies

The microscopic examinations discover that the fracture surfaces exhibit fairly complex morphologies. Five failure modes are observed; interface crack, in-ply crack, crack jumping, fiber bridging and fiber breakage. Even inside the specimens with the same lay-up, different failure modes are also observed. Tables 1 and 2 list the specimen numbers with respective failure modes observed in the testing.

**Table 1.** Specimen numbers with different failure modes; for the  $S_{13}$  at the 0/ $\theta$  interfaces.

$\theta$	0°	10°	20°	30°	40°	50°	60°	70°	80°	90°
Interface crack	7	15	27	22	18	20	19	29	12	16
In-ply crack	4	8	3	2		3			23	
Crack jumping	24	12	5	3	3	3		4		13
Fiber bridging							2	2		6
Fiber breakage				8	14	9	14			

**Table 2.** Specimen numbers with different failure modes; for the  $S_{23}$  at the 90/(90- $\theta$ ) interfaces.

$\theta$	0°	10°	20°	30°	40°	50°	60°	70°	80°
Interface crack			2			1		13	16
Crack jumping	14	11	15	20	12	18	11	10	11
Fiber bridging	21	24	18	15	23	16	24	12	8

The fracture surface morphologies of the 0/ $\theta$  interfaces are typically demonstrated in Fig. 6. The failure mode of interface crack is expected because the cracks always grow along the interfaces, thereby providing the pure delamination failure. The fracture surfaces exhibit matted morphologies and distinct straight streaks along the 0° and  $\theta$  directions can be observed by naked eyes. The failure mode of in-ply crack defines the cracks that propagate within one single ply parallel to the interfaces. The in-ply cracks are always found to grow in the 0° plies. It can be seen by naked eyes that the fracture surfaces exhibit glossy morphologies. In most cases, the in-ply cracks are formed at locations very close to the interfaces so that narrow interface strips are still observed, as shown by the white line in Fig. 6(b). The failure mode of crack jumping is formed through the transverse matrix cracks, and always accompanied by the interface crack or in-ply crack. In the failure mode of fiber bridging, the bridged fibers could increase the ILS strengths [4]. Sometimes, the fiber breakage happens if the external load is suspended by the bridged fibers before the final failure, which is thus a mark of fiber bridging [4]. Therefore, there is no fiber breakage at the initiation of delamination. It can be seen that the failure mode of fiber

breakage is accompanied by the crack jumping across one  $\theta$  ply, and always occurs in the  $\theta$  plies. The broken fiber edges are found to be neat and normal to the fiber directions. Hence, the  $S_{13}$  is higher at the 0/30, 0/40, 0/50 and 0/60 interfaces as well as the 0/90 interfaces, because a number of specimens exhibit the fiber bridging, or the fiber breakage.

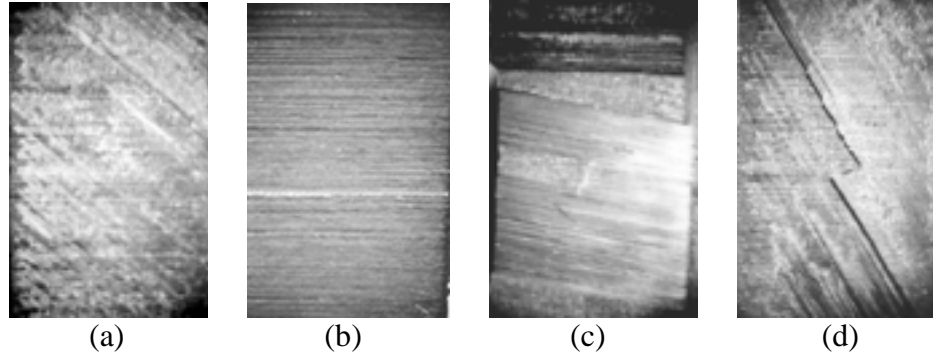


**Fig. 6.** Failure modes in Type I specimens; a) interface crack at 0/50 interface, b) in-ply crack near 0/20 interface, c) crack jumping at 0/10 interface, and d) fiber breakage at 0/60 interface.

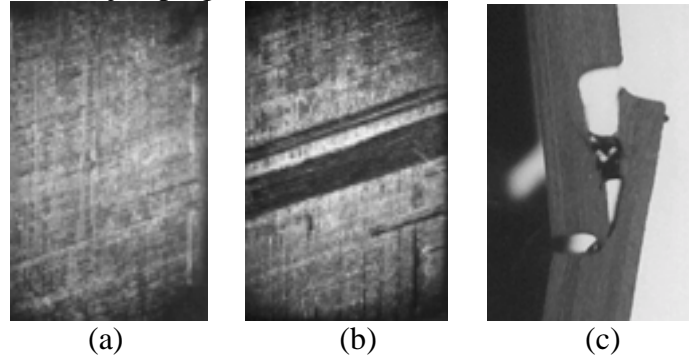


**Fig. 7.** Failure modes in Type II specimens; a) interface crack at the 90/20 interface, (b) crack jumping at 90/20 interface, and c) fiber bridging at 90/50 interface.

Different from those in the Type I specimens, there are only three failure modes with the Type II specimens; i.e., interface crack, crack jumping and fiber bridging, as shown in Fig. 7. Accordingly, the ILS strengths  $S_{23}$  present small  $C_v$ . Except for the specimens with the 90/20 ( $\theta = 70^\circ$ ) and 90/10 ( $\theta = 80^\circ$ ) interfaces, the other specimens almost fail only in the failure modes of crack jumping or fiber bridging. At the fracture surfaces with the failure mode of interface crack, the straight streaks along the  $90^\circ$  and  $(90^\circ - \theta)$  directions are also apparent. The failure mode of crack jumping in the Type II specimens involves at least one interface; growing from interface crack to interface crack through the transverse matrix cracks across the adjacent plies or deviating from interface crack to in-ply crack. Large number of specimens with each specified interface has the failure mode of fiber bridging, because the  $90^\circ$  plies give an obstacle to the delamination growth, thus increasing the  $S_{23}$ . Moreover, the fiber bridging usually accompanied with the crack jumping would make delamination tend to propagate around the  $90^\circ$  plies, therefore promoting the delamination growth along two interfaces [4].

### 3. STOCHASTIC MODELING

Our experimental results present that the ILS strengths have two distinct characteristics; 1) the strength values present considerable scatter, and 2) the mean values and probability distribution forms depend on the magnitude of the FOD angle  $\theta$ . These probabilistic

characteristics need to be thoroughly known in the design of composite structures on the basis of the reliability-based methodology. The analytical modeling becomes imperative to obtain the probabilistic characteristics in the whole domain of the FOD angles (i.e.,  $0 \leq \theta \leq \pi/2$ ) based on those at a limited number of discrete FOD angles. The stochastic simulation technique, in which the ILS strengths are simulated as a stochastic process with respect to  $\theta$ , could be an efficient method. The purpose of the stochastic modeling is to establish the simulation algorithm in order to obtain the stochastic processes  $S_{13}(\theta)$  and  $S_{23}(\theta)$  that can satisfy all the probabilistic characteristics (up to the fourth order) of the experimental data sets at the 10 discrete values of  $\theta$ , and thus the probabilistic characteristics at the FOD angles at which the experiments are not performed could be available.

So far numerous simulation techniques have been well established towards the Gaussian stochastic processes, but no simulation approaches have been developed towards the non-Gaussian processes with probability distribution forms varying with the spatial or time variables. Herein, a simulation algorithm is proposed towards the stochastic processes with very general probabilistic characteristics, as those in the processes  $S_{13}(\theta)$  and  $S_{23}(\theta)$ . This attempt is implemented by approximating the stochastic processes within the bounded interval  $[0, \pi/2]$  to the trigonometric polynomials in terms of the correlated non-Gaussian random coefficients.

### 1) SIMULATION ALGORITHM

Suppose that the nonstationary stochastic process  $S(\theta)$  can be approximately represented by a 10<sup>th</sup> order of Fourier cosine series in the interval  $[0, \pi/2]$  (here the order is determined by the number of discrete FOD angles at which experiments are performed) [13],

$$S(\theta) = \frac{A_0}{2} + \sum_{i=1}^9 A_i \cos \omega_i \theta \quad (3)$$

where  $A_i$ 's are correlated random coefficients and  $\omega_i = 2i$ . The analytical expressions for the 1<sup>th</sup>, 2<sup>th</sup>, 3<sup>th</sup> and 4<sup>th</sup> joint moments of the stochastic process  $S(\theta)$  can be derived in terms of the joint moments of the random variables  $A_i$ 's based on Equ 3, that is,

$$E[S(\theta)] = E\left(\frac{A_0}{2}\right) + \sum_{i=1}^9 E(A_i) \cos \omega_i \theta \quad (4)$$

$$k(t, \tau) = E[(S(t)S(\tau))] = E\left[\frac{A_0^2}{4}\right] + \sum_{i=1}^9 E\left(\frac{A_0}{2} A_i\right)(\cos \omega_i t + \cos \omega_i \tau) + \sum_{i=1}^9 \sum_{j=1}^9 (A_i A_j) \cos \omega_i t \cos \omega_j \tau \quad (5)$$

$$\begin{aligned} k(t, \tau, s) = E[(S(t)S(\tau)S(s))] = & E\left(\frac{A_0^3}{8}\right) + \sum_{i=1}^9 E\left(\frac{A_0^2}{2} A_i\right)(\cos \omega_i t + \cos \omega_i \tau + \cos \omega_i s) \\ & + \sum_{i=1}^9 \sum_{j=1}^9 \left(\frac{A_0}{2} A_i A_j\right)(\cos \omega_i t \cos \omega_j \tau + \cos \omega_i \tau \cos \omega_j s + \cos \omega_i s \cos \omega_j t) \\ & + \sum_{i=1}^9 \sum_{j=1}^9 \sum_{k=1}^9 E(A_i A_j A_k) \cos \omega_i t \cos \omega_j \tau \cos \omega_k s \end{aligned} \quad (6)$$



$$\begin{aligned}
k(t, \tau, s, \sigma) &= E[(S(t)S(\tau)S(s)S(\sigma))] = E\left(\frac{A_0^4}{16}\right) + \sum_{i=1}^9 E\left(\frac{A_0^3}{3} A_i\right)(\cos \omega_i t + \cos \omega_i \tau + \cos \omega_i s + \cos \omega_i \sigma) \\
&+ \sum_{i=1}^9 \sum_{j=1}^9 \left(\frac{A_0^2}{2} A_i A_j\right)(\cos \omega_i t \cos \omega_j \tau + \cos \omega_i t \cos \omega_j s + \cos \omega_i t \cos \omega_j \sigma + \cos \omega_i \tau \cos \omega_j s \\
&+ \cos \omega_i \tau \cos \omega_j \sigma + \cos \omega_i s \cos \omega_j \sigma) + \sum_{i=1}^9 \sum_{j=1}^9 \sum_{k=1}^9 E\left(\frac{A_0}{2} A_i A_j A_k\right)(\cos \omega_i t \cos \omega_j \tau \cos \omega_k s \\
&+ \cos \omega_i t \cos \omega_j \tau \cos \omega_k \sigma + \cos \omega_i t \cos \omega_j s \cos \omega_k \sigma + \cos \omega_i \tau \cos \omega_j s \cos \omega_k \sigma) \\
&+ \sum_{i=1}^9 \sum_{j=1}^9 \sum_{k=1}^9 \sum_{l=1}^9 E(A_i A_j A_k A_l) \cos \omega_i t \cos \omega_j \tau \cos \omega_k s \cos \omega_l \sigma
\end{aligned} \tag{7}$$

Therefore, if the joint moments of  $A_i$ 's are known, those of  $S(\theta)$  can also be determined. The joint moments of  $S(\theta)$  between the ILS strengths at 10 discrete FOD angles can be estimated from the experimental data sets, which are then substituted into Eqs 4 to 7. Four sets of linear homogeneous equations are established regarding the joint moments of  $A_i$ 's up to the fourth order, which are then obtained by solving the equation sets respectively. At this point, all the joint moments of  $S(\theta)$  in the interval  $[0, \pi/2]$  are determined.

## 2) BOUND ESTIMATION

The lower and higher bounds of the stochastic process  $S(\theta)$  in the whole domain are essential to evaluate the individual pdfs using the maximum entropy technique. In the present stochastic modeling, an estimation method is also developed based on the time series theory [14] by assuming each bound sample data to be a stationary time series  $z$  with respect to  $\theta$ . So there are only ten sample data corresponding to the 10 specified FOD angles  $\theta_k$  in each time series  $z(\theta)$ . The involved purpose is to obtain the bounds in the whole domain based on the 10 experimental data by performing the stochastic interpolation. The value  $z(\theta_k + \Delta\theta)$  can be estimated in terms of the three sample data that are nearest to  $\theta_k$  [14],

$$\hat{z}(\theta_k + \Delta\theta) = \sum_{i=k-1}^{k+1} a_i z(\theta_i) \tag{8}$$

where more terms would be preferable so as to yield the better estimation, but we only employ three sample data for the convenience of calculating. On the basis of the orthogonality principle,

$$E\left\{\left[z(\theta_k + \Delta\theta) - \sum_{i=k-1}^{k+1} a_i z(\theta_i)\right] z(\theta_j)\right\} = 0 \quad k-1 \leq j \leq k+1 \tag{9}$$

one can derive that

$$\sum_{i=k-1}^{k+1} a_i R(\theta_i - \theta_j) = R(\theta_k + \Delta\theta - \theta_j) \quad k-1 \leq j \leq k+1 \tag{10}$$

Thus,  $a_i$ 's can be obtained by the third order linear homogeneous equation set provided that the autocorrelation function  $R(\tau)$  is known, which can be estimated as follows. The mean and the autocovariance of the time series  $z(\theta)$  can be estimated by

$$\mu = \frac{1}{10} \sum_{i=1}^{10} z_i; \quad c_k = \frac{1}{10} \sum_{i=1}^{10-k} (z_i - \mu)(z_{i+k} - \mu) \tag{11}$$

The sample spectrum  $c(\omega)$  can thus be written in terms of the  $c_k$  [15]

$$c(\omega) = \Delta[c_0 + 2 \sum_{i=1}^2 c_i \cos(2\pi\omega i\Delta)] \quad -1/(2\Delta) \leq \omega \leq 1/(2\Delta) \tag{12}$$

where  $\Delta = \pi/18$  (the difference between two neighboring discrete FOD angles). From the inverse Fourier transform of the spectrum, one can obtain the estimation of the autocorrelation function.

$$R(\tau) = \int_{-1/2\Delta}^{1/2\Delta} c(\omega) \exp(j2\pi\omega\tau) d\omega + \mu \quad (13)$$

### 3) NUMERICAL RESULTS

Based on the simulation algorithm, the moments and the bounds can be estimated in the whole domain. Then the individual pdfs can be evaluated at any FOD angle by the maximum entropy technique. The pdfs of the  $S_{13}$  at the 0/45 interface and the  $S_{23}$  at the 90/15 interfaces are shown in Fig. 8. Also included are the pdfs at the nearest FOD angles that are estimated from the experimental data sets. Further numerical results are not demonstrated due to space limitation.

### 4. CONCLUSIONS

The probabilistic characteristics involving the dependence of ILS strengths on the FOD angles are experimentally and analytically investigated. These characteristics can be incorporated into the reliability evaluation of laminated composites governed by the out-of-plane failure mode based on appropriate failure criteria. The fracture surface morphologies of the double notch shear specimens present five failure modes; i.e., interface crack, in-ply crack, crack jumping, fiber bridging and fiber breakage. The ILS strengths exhibit considerable scatter, and both the mean values and probability distribution forms are changed with the FOD angles  $\theta$ .

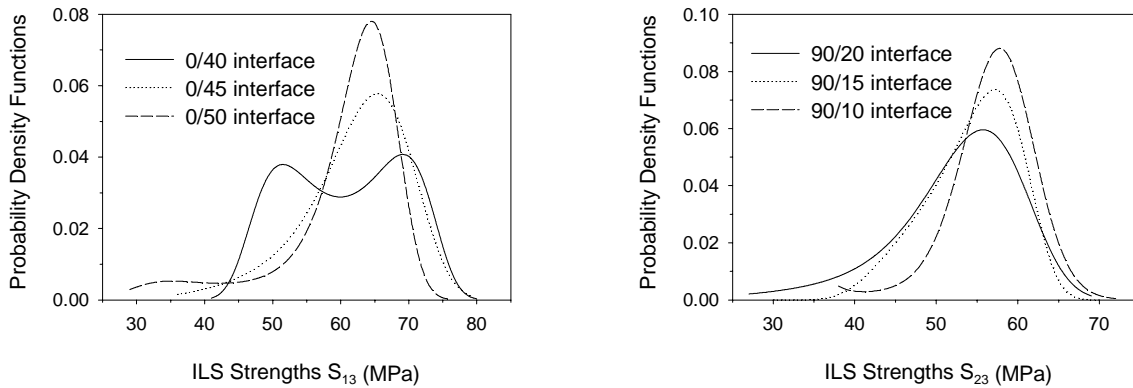


**Fig. 8.** Probability density functions of the  $S_{13}$  and  $S_{23}$ ; those at the 0/45 and 90/15 interfaces are calculated using the stochastic simulation algorithm.

### REFERENCES

- [1] Zhang, C., Hoa, S. V. and Ganesan, R., "Edge Effects in Laminated Composites with Pin-Loaded Holes," *AIAA Journal*, Vol. 36, 1998, pp. 1883-1893.
- [2] Zhang, C., Ganesan, R. and Hoa, S. V., "Interlaminar Stresses in Quasi-Isotropic Laminated Composites with Circular Cutouts," *AIAA Journal*, in review, 1998.
- [3] Zhang, C., Ganesan, R. and Hoa, S. V., "Effects of Friction on Three-Dimensional Contact Stresses in Pin-Loaded Laminated Composites," *Journal of Composites Materials*, in review, 1999.
- [4] Chou, I., Kimpara, I., Kageyama, K. and Ohsawa, I., "Mode I and Mode II Fracture Toughness on Differently Oriented Interlaminar in Graphite/Epoxy Composites," *Composite Materials: Fatigue and Fracture, ASTM STP 1230*, 1995, pp. 132-151.
- [5] Tao, J. and Sun, C. T., "Influence of Ply Orientation on Delamination in Composite Laminates," *Journal of Composite Materials*, Vol. 32, 1998, pp. 1933-1947.
- [6] Russell, A. J. and Street, K. N., "Factors Affecting the Interlaminar Fracture Energy of Graphite/Epoxy Laminates," *ICCM-4*, Tokyo, 1982, pp. 279-286.
- [7] Davidson, B. D., Altonen, C. S. and Polaha, J. J., "Effect of Stacking Sequence on Delamination Toughness and Delamination Growth Behaviour in Composite End-Notched Flexure Specimens," *Composite Materials: Testing and Design, ASTM STP 1274*, 1994, pp. 393-413.
- [8] Sun, C. T. and Zhou, S. G., "Failure of Quasi-Isotropic Composite Laminates with Free Edges," *Journal of Reinforced Plastics and Composites*, Vol. 7, 1988, pp. 515-557.

- [9] Chiao, C. C., Moore, R. L. and Chiao, T. T., "Measurement of Shear Properties of Fibre Composites: Part I – Evaluation of Test Methods," *Composites*, Vol. 8, 1977, pp. 161-169.
- [10] Shokrieh, M. M., Olivia, P. E., Kotsioprifits, P. and Lessard, L. B., "Determination of Interlaminar Shear Strength of Graphite/Epoxy Composite Materials in Static and Fatigue Loading," *ICCM-10*, Vancouver, 1995, IV-81-88.
- [11] Swason Analysis Systems, INC., *ANSYS User's Manual*, Version 5, 1992.
- [12] Siddall, J. N., *Probabilistic Engineering Design: Principles and Applications*, Marcel Dekker, Inc., New York, 1983.
- [13] Grigoriu, M., "Simulation of Nonstationary Gaussian Processes by Random Trigonometric Polynomials," *Journal of Engineering Mechanics*, Vol. 119, 1993, pp. 328-343.
- [14] Papoulis, A., *Probability, Random Variables, and Stochastic Processes*, Second Edition, McGraw-Hill, Inc., New York, 1984.
- [15] Jenkins, G. M. and Watts, D.G., *Spectral Analysis and Its Applications*, Holden-Day, Inc., San Francisco, 1968.